High-throughput two-photon volumetric brain imaging in freely moving mice

Long Qian[1,2,4], Yaling Liu[1,2,4], Yalan Chen[2,3], Jianglai Wu[1,2]*

[1]Beijing Institute for Brain Research, Chinese Academy of Medical Sciences & Peking Union Medical College, Beijing, 102206, China

[2]Chinese Institute for Brain Research, Beijing 102206, China

[3]State Key Laboratory of Cognitive Neuroscience and Learning, Beijing Normal University, Beijing, 100875, China

[4]These authors contributed equally: Long Qian and Yaling Liu

*Corresponding author: wujianglai@cibr.ac.cn

Imaging neural activities across large volumes at subcellular resolution without impeding animal behaviors remains difficult. Here we introduce a high-throughput miniature Bessel-beam two-photon microscope capable of imaging calcium dynamics from neurons and dendrites over a volume of 420 × 420 × 80 μm³ during free behavior. We share full description of the microscope and demonstrate calcium imaging of more than 1000 neurons at a time in freely moving mice.

Head-mounted miniature multiphoton microscopy offers a promising avenue for investigating neural activity during free and naturalistic behavior in mice and rats, thanks to its inherent optical sectioning and deep tissue penetration capabilities [1]. Recent advancements in optical fibers, miniature detectors, focus-tunable lenses, and objectives have significantly improved the performance of miniature multiphoton microscopes [2-10], leading to a substantial increase in the number of neurons that can be imaged in freely moving animals in practical neurobiological investigations [10-13]. However, several limitations are presented in existing miniature multiphoton microscopes. First, rapid volumetric imaging is challenging due to the sequential acquisition of each voxel, especially when using high numerical aperture (NA) objectives that offer superior lateral and axial resolution. While advanced platforms with fast focus-tunable lenses can scan the focus axially in milliseconds [5,10], a restricted number of thin optical sections within a volume can be imaged at a time, albeit at the expense of imaging speed and resolution. Second, the shallow depth of field of the microscope makes imaging susceptible to brain tissue movement, particularly axial movement. This issue is a common concern in imaging head-fixed animals [14] and would be exacerbated when imaging freely moving animals as brain movement is less constrained [1]. Finally, while customized optics such as miniature objectives have been utilized to achieve higher resolution and larger field of view (FOV), achieving diffraction-limited resolution across the FOV remains difficult [6, 8, 10]. This challenge arises from the need to fit all optics into a compact space of a few cubic centimeters, which poses extra hurdles for lens design and assembly.

Bessel beam can address these limitations. In recent years, tabletop two-photon microscopes (2PM) utilizing Bessel beams have shown several distinct features over the widely used Gaussian beams [15-20]. Bessel-beam 2PM captures projected views of volume structures by scanning an axially elongated focus in 2D. This process transfers the 2D scan rate into a volumetric imaging rate, increases the information throughput, and reduces the data size. The extended depth of field makes imaging resistant to axial movements of brain tissue [17], which is preferred in monitoring neural circuits in freely moving animals. Moreover, Bessel-beam 2PM achieves better lateral resolution than Gaussian-beam 2PM at same excitation NA [17-18] and is insensitive to optical aberrations such as spherical aberration and coma, indicating the potential of designing simple lenses for miniature microscopes [20-21]. In this work, taking advantage of these unique features, we developed a high-throughput miniature Bessel-beam two-photon microscope (miniBB2p) for freely moving mice research (**Figs.1a-e, Supplementary Fig. 1 and Methods**).

Among all primary optical aberrations, Bessel beam is mainly sensitive to astigmatism [20-21]. Leveraging this characteristic, we utilized a systematic approach in miniBB2p to eliminate astigmatism while minimizing other primary aberrations. Briefly, we adopted a symmetric design for the scan and tube lenses, each comprising two identical plano-convex lenses (**Supplementary Fig. 2a**). This symmetry minimizes coma, distortion, and lateral color aberration. Uncorrected astigmatism was fully compensated by the objective formed by two plano-convex lenses (**Supplementary Fig. 2b**). In parallel, other aberrations in the objective were well-contained under the low excitation NA of 0.3, leading to near-diffraction-limited performance over a FOV of Ø 600 μm (**Supplementary Fig. 2c**). Throughout the entire FOV, we noted negligible blurring of the Bessel focus from the residual spherical aberration and coma, in contrast to the blurring observed with a Gaussian focus (**Supplementary Fig. 3**).

We used a 1-meter large-mode-area photonic crystal fiber (LMA-12, NKT Photonics) to transmit the 920-nm femtosecond laser pulses for two-photon excitation. To generate the Bessel beam, we engineered a custom micro-axicon at the fiber tip **(Fig. 1b, Supplementary Fig. 1c and Methods)**. A microelectromechanical systems (MEMS) mirror was used as the scanner, enabling a maximum square FOV of 420 × 420 μm^2 and a frame size of 512 × 512 pixels at 9 frames per second. The miniBB2p featured a working distance of 1 mm in water, an excitation NA of 0.26, and a collection NA of 0.95. Lateral and axial resolution measured with fluorescent beads were 0.97–0.99 μm and 80–90 μm across the FOV (**Supplementary Fig. 5**). The lateral resolution obtained is equivalent to diffraction-limited resolution using a Gaussian beam at a higher NA of 0.35. Notably, fluorescence collection efficiency is 2–4 times greater than that in the state-of-the-art platforms with a comparable FOV and lateral resolution [8-10] (**Supplementary Figs. 4a-d and Supplementary Table 1**). In addition, fluorescence

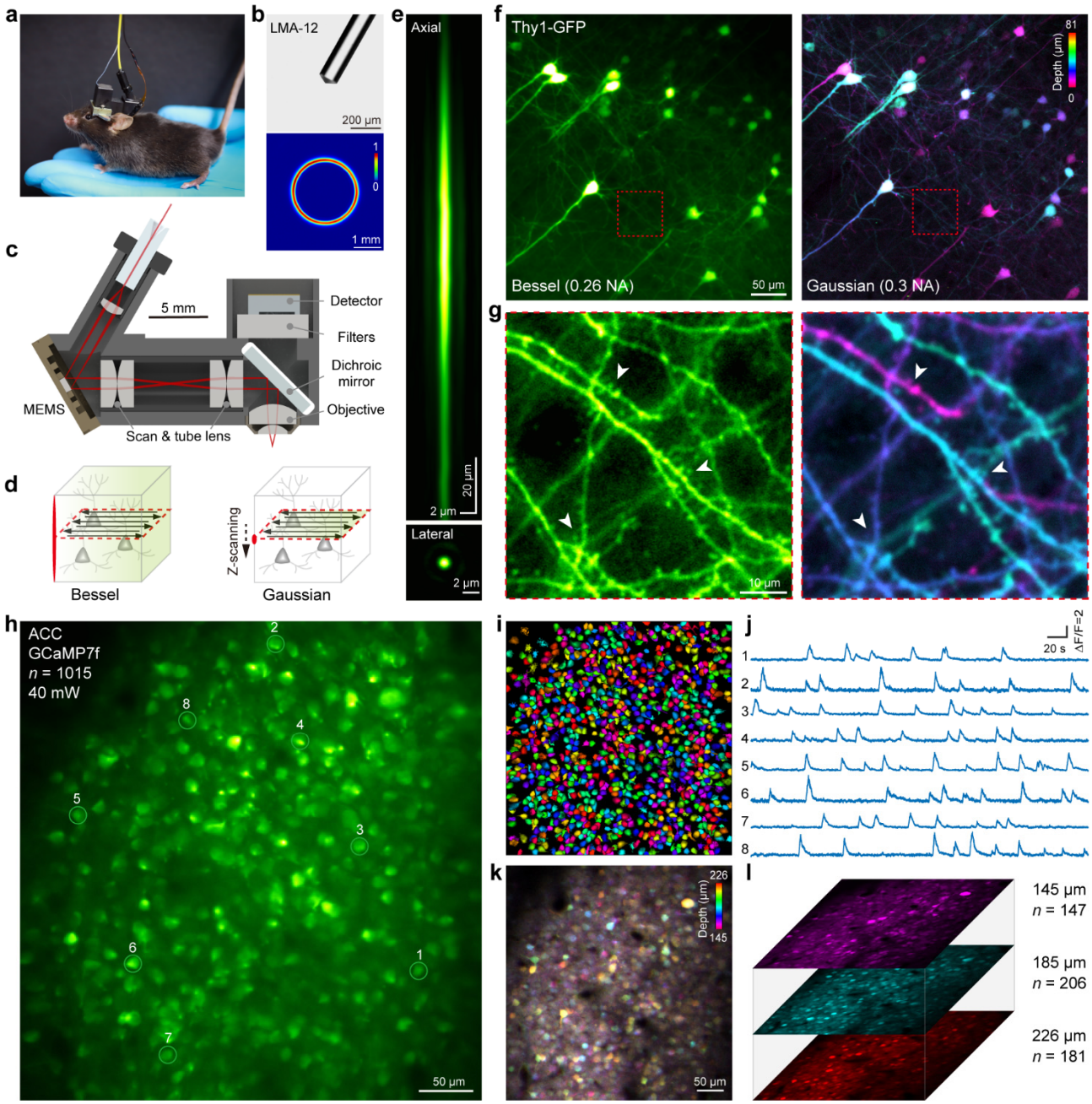

Fig. 1 | Design and test of miniBB2p. a, Photograph of a mouse wearing the microscope headpiece. **b**, Brightfield micrograph of the custom micro-axicon at the LMA-12 fiber tip (top) and ring pattern imaged at ~5-mm distance from the fiber tip (bottom). **c**, Schematic of miniBB2p showing key elements and excitation beam path (red lines). **d**, Imaging a volume requires a single 2D scan of a Bessel focus but a stack of 2D scans of a Gaussian focus. **e**, Lateral and axial point spread functions measured with 500-nm fluorescent beads. **f**, Image of a ~80-µm thick volume of Thy1-GFP-M brain slice by miniBB2p (left) and an image stack at 3-µm step collected by a tabletop Gaussian beam 2PM from the same volume, with structures colored by depth (right). **g**, zoom-in imaging of the boxed areas in **f**; white arrowheads denote dendritic spines that were more clearly visualized by Bessel focus. **h**, Imaging the spontaneous activity of neurons in anterior cingulate cortex (ACC) expressing GCaMP7f in a free-moving mouse with miniBB2p. **i**, Spatial distribution of 1015 neurons extracted by *Suite2P* in **h**, randomly colored for visualization. **j**, Example calcium signals from neurons circled in **h**. **k-l**, Imaging the same volume in awake head-fixed mouse by the tabletop 2PM: Gaussian imaging stack at 3-µm step with structures colored by depth (**k**); neural activity imaging in the top, middle, and bottom layers of the volume, the imaging depth and number of neurons identified by *Suite2P* are listed at right (**l**).

was directly detected after the objective and filters using an onboard silicon photomultiplier, which offered higher detection efficiency and less tethered burden than fluorescence collection using thick fibers as a relay unit [6]. Total weight of the assembled microscope headpiece was 2.6 g. Mounting the headpiece along with the fiber and cables did not significantly impede the movement of mice **(Supplementary Fig. 6)** and same volume could be pinpointed and imaged in experiments conducted on different days **(Supplementary Fig. 7)**.

We first imaged Thy1-GFP-M mouse brain slices to demonstrate the throughput and resolution of miniBB2p (**Figs. 1f-g**). Using a commercial tabletop Gaussian-beam 2PM (0.3 NA, axial resolution 22.9 μm), a stack of at least 4 images is required to cover all structures within an 80-μm thick volume. In comparison, miniBB2p captured the same information in one image, increasing the throughput by a factor of 4. Moreover, the higher resolution in Bessel focus allowed easier visualization of dendritic spines (**Fig. 1g**). These observations were also found in head-fixed mouse brain **(Supplementary Fig. 8)**. We then employed miniBB2p to image spontaneous neural activities in freely moving mice. We resolved calcium dynamics of 1015 neurons at a time in the anterior cingulate cortex (ACC) **(Figs. 1h-j and Supplementary Video 1)**. This result was validated through structural imaging at same region and neural activity imaging in the top, middle, and bottom layers within same volume using the tabletop 2PM on head-fixed mice (**Figs. 1k-l**). The latter approach identified 534 neurons across the three layers, half the number resolved with miniBB2p. Beyond that, miniBB2p was able to image calcium transients in dendritic trees and spines along multiple dendritic branches in an axially extended volume (**Supplementary Fig. 9 and Supplementary Videos 2-3**). These measurements underscored the benefits of high-resolution volumetric imaging.

We next investigated the response of pyramidal neurons in secondary motor cortex (M2) to locomotion during a 30-minute recording while the mice freely explored the behavior arena (**Figs. 2a-c and Supplementary Video 4**). Running increased the mean ΔF/F in most neurons, with a running modulation index (MI) showing increased activity during running (**Figs.2d-e**; n=878 neurons, running MI 0.156 ± 0.006, mean ± s.e.m.). In addition, we inspected the average fluorescence changes aligned with running onsets and found that approximately 38% of the neurons significantly increased their activities upon running onset (**Fig. 2f and Methods**), resembling the study from recordings in primary somatosensory cortex (S1) [22].

Last, we examined the neural activity in ACC under different pain stimulation paradigms in freely moving mice. We imaged the Ca^{2+} activity of 673 ± 104 (5 mice, mean ± s.e.m.) pyramidal neurons both before and after administrating a peripheral stimulus (**Figs. 2g-h, Supplementary Video 5 and Methods**). Following the noxious 27 G pin prick stimulus, these neurons exhibited higher Ca^{2+} activity compared to the non-noxious 0.4g von-Frey filament

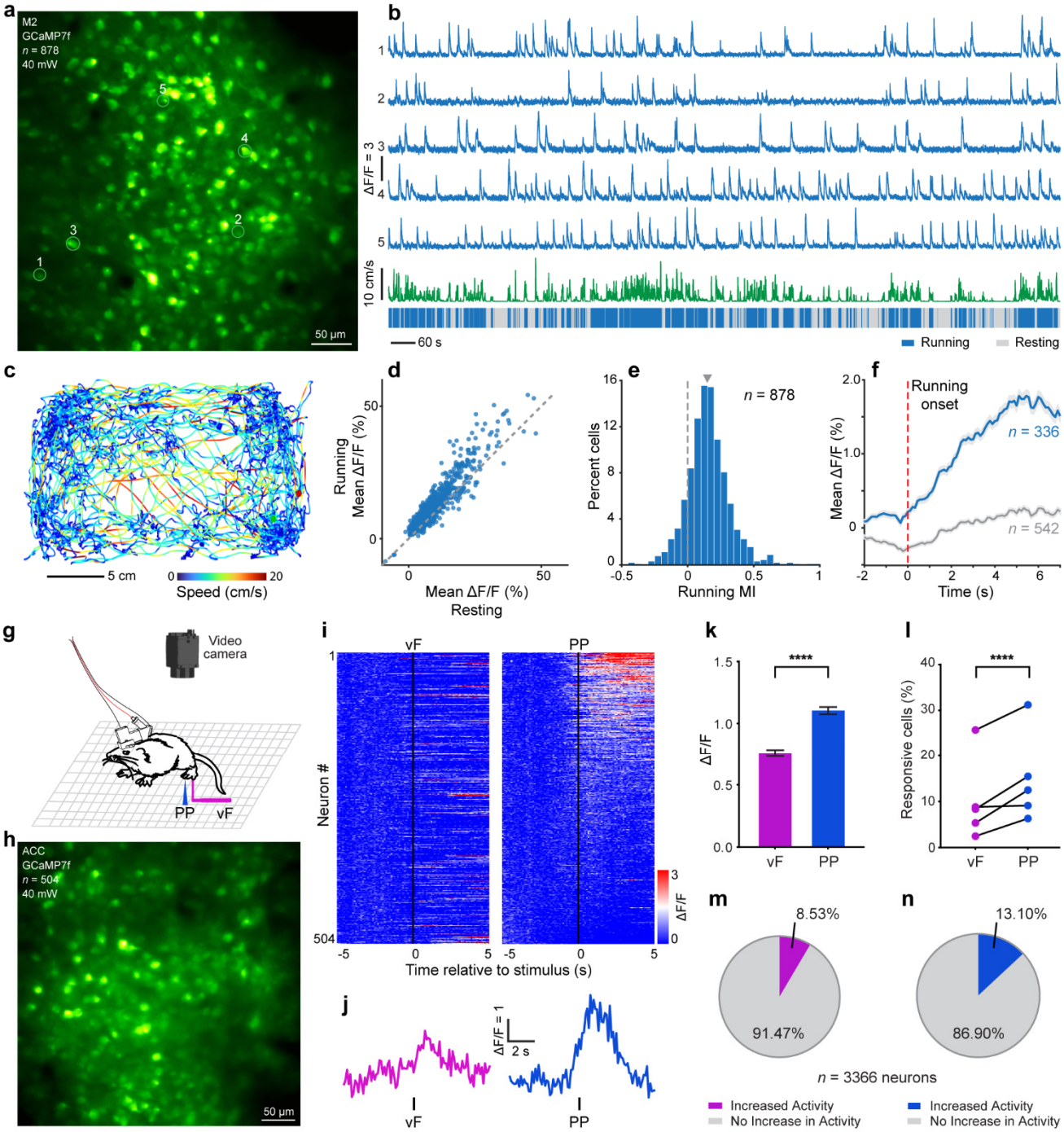

Fig. 2 | Demonstrations of miniBB2p. a-f, Recordings in M2. **a**, Image of an example neuronal population in M2. **b**, Representative calcium traces along with moving speed from neurons circled in **a**; running and resting states are color coded with blue and gray. **c**, Movement trajectory and speed of the mouse over a 30-minute recording period. **d**, Scatter plot of the mean ΔF/F values in resting and running states for the 878 neurons recorded; dashed line indicates a unity line. **e**, Distribution of running modulation index for the neurons; triangle indicates median. **f**, Population average of ΔF/F traces for neurons with and without increasing Ca^{+} activity in response to the running onset (16 events), shaded areas indicate s.e.m. **g-l**, Recordings in ACC. **g**, Schematic diagram for monitoring the response of ACC neurons to noxious (PP, pin prick) or non-noxious (vF, 0.4 g vF filament) stimulus in freely moving mice. **h**, Image of an example neuronal population in ACC. **i**, Z-scored mean ΔF/F across all trials (n = 5) for 504 neurons recorded from the example mice. Neurons are aligned from high to low Ca^{2+} responses after PP stimulus. **j**, Representative trace of z-scored mean Ca^{2+} response of a single neuron during vF and PP. **k**, PP induced a higher Ca^{2+} response than vF (mean ± s.e.m.); $p < 0.0001$, paired Student's t test. **l-n**, More neurons increased activity in response to PP compared to vF, $p < 0.0001$, Fishers exact test (**l**); 8.53% and 13.10% of the neurons showed a change in activity in response to vF (**m**) and PP (**n**) stimulus (n = 3366 neurons in 5 mice).

stimulus (**Figs. 2i-k**). Furthermore, more neurons responded to the noxious stimulus than to the non-noxious stimulus (**Figs. 2l-n**). These observations are consistent with previous studies showing increased firing rates in ACC neurons during noxious stimuli [23-24]. We also imaged Ca^{2+} activity of interneurons in ACC upon receiving pin prick stimulus, both before and after chemogenetic inhibition of neural activity in S1 (**Supplementary Fig. 10 and Methods**). The interneurons in ACC became more sensitive to pin prick after the inactivation of S1, suggesting they receive nociceptive information from S1 [24]. This relationship highlights the role of these neurons in processing the sensory and affective aspects of pain.

In summary, we developed miniBB2p for high-resolution and high-throughput volumetric calcium imaging of more than 1000 neurons at a time in freely moving mice. The miniBB2p featured a lightweight, reduced tethering stress, simple optics, and maximized fluorescence collection efficiency. These strengths allowed long-term stable imaging without impeding the animal behavior, using a safe laser power (40–100 mW) comparable to that used in tabletop Bessel beam 2PMs (**Supplementary Table 2**) [17]. Higher throughput could be realized by integrating a rapid axial scanning unit into miniBB2p for volumetric imaging across multiple depths [5, 10]. While the large-mode-area fiber used in this work can effectively deliver femtosecond laser pulses from 700 to1700 nm, a promising feature for imaging indicators with different excitation wavelengths, we noted that the pulse is substantially broadened at high power due to nonlinear effects within the fiber (**Supplementary Fig. 1b**). This shortcoming would compromise performance of the microscope when utilizing a power exceeding 100 mW. Future developments using hollow-core photonic bandgap fiber (HC-920, NKT Photonics) can address this issue and further enhance the sensitivity in imaging GFP-based indicators [2].

We developed minBB2p to be cost-effective without impairing its capability. Using readily available off-the-shelf lenses, the whole microscope headpiece can be built for less than 2500 US dollars (**Supplementary Table 3**). In addition, the simple optical design allowed us to assemble the optics to approach the diffraction limit. We anticipate that the design's simplicity and cost-effectiveness will diminish the barriers to a broader application of head-mounted multiphoton microscopy for studying neural dynamics in freely moving animals. Moreover, the optical design methodologies established in this study may pave the way for future advancements in miniature multiphoton microscopes with a larger FOV and higher resolution.

METHODS

Microscope setup and system control. A fiber-based femtosecond laser (FemtoFiber ultra 920, Toptica) with a built-in dispersion precompensation unit (-40000 to +1000 fs^2) was used to produce laser pulses at a center wavelength of 920 nm (920±10 nm, 100 fs, 80 MHz, 1.2 W). Using an objective (LMPLFLN20×, Olympus), the laser was coupled into the LMA-12 fiber. The pulse in the fiber was broadened by material dispersion and nonlinear effects. Dispersion from the 1-meter fiber was fully compensated with the precompensation parameter set to -26000 fs^2. Benefitting from the large mode area (~Ø10 μm), nonlinear effects in the fiber were substantially reduced. The optimized pulse width was less than 200 fs at laser powers below 40 mW and less than 300 fs at laser powers below 100 mW (**Supplementary Fig. 1b**).

In miniBB2p, fiber tip with the custom axicon was aligned with a collimating lens (45-956, Edmund Optics) to generate the ring-shaped beam. The MEMS scanner (A3I12.2-1200AL, Mirrorcle) provided a 1.2-mm diameter mirror with the first resonant frequency of both axes at ~2.6 kHz and it was used at a 30° incidence angle. After the scan lens and tube lens, which were formed by four identical plano-convex lenses (48-704, Edmund Optics) in a symmetrical configuration, a dichroic mirror (7 × 7 mm^2, 1 mm thick; DMR-805SP, LBTEK) was used to separate the laser beam and fluorescence. The objective, consisting of two plano-convex lenses (47-850 and 65-300, Edmund Optics), was used to generate the Bessel focus in the specimen. Fluorescence was collected through the objective, dichroic mirror, and filters, and was detected with an onboard miniature, low-cost silicon photomultiplier (3 × 3 mm^2, S13360-3075PE, Hamamatsu). A reflective filter (6 × 6 mm^2, 0.2 mm thick; 450–650 nm transmission, FIL-800, Sunlight) and a colored glass filter (6 × 6 mm^2, 2 mm thick; FGB37-A, Thorlabs) were placed before the detector to reject the strong infrared laser. The microscope housing was made of carbon-fiber-enhanced plastic (PEEK-CF30) to reduce the weight of the headpiece.

The control signals for x-y scanning were generated from a MEMS controller (USB-SL MZ, Mirrorcle), which was also used to drive the acousto-optic modulator in the laser for power control and to trigger the data acquisition. The scanner was operated in resonance mode along the x-axis at 2304 Hz, scanning 4608 lines every second in bi-directional mode. This operation resulted in an image of 512 × 512 pixels at 9 frames per second. The x-axis scanning range was about $\sqrt{2}$ times the y-axis scanning range to achieve a nearly square FOV [10]. The silicon photomultiplier was wired by a thin coaxial cable (Ø 260 μm) to the driver circuit (C12332-01, Hamamatsu). Fluorescence signal was amplified by the same circuit and sampled with a digitizer (20 MS/s, M2p.5921-x4, Spectrum Instrumentation). The entire system was controlled by custom software based on the MATLAB (R2022a) platform.

Micro-axicon design. We customized a micro-axicon at the tip of the LMA-12 fiber (Comcore, China). Specifically, the tip of the photonic crystal fiber was collapsed and polished to form an

axicon lens with an apex angle of 120°. The laser from the photonic crystal region in the fiber was spread out at the collapsed region (~1 mm length) and transformed into a diverged ring beam by the axicon (**Supplementary Fig. 1c**). After the collimating lens, a focused ring beam was generated at the back focal plane of the scan lens, where the MEMS mirror was located. The maximum diameter of the ring beam that the mirror can accommodate is 1 mm, corresponding to a maximum excitation NA of 0.3. In this work, the diameter of the ring beam was measured to be 0.85 mm and it resulted in an excitation NA of 0.26.

Resolution and FOV calibration. We ascertained the resolution of miniBB2p by imaging 500-nm fluorescent beads (F8813, Thermo Fisher Scientific), with a pixel size of 0.1 μm to measure lateral resolution and an axial step size of 6 μm to measure axial resolution. The resolutions were evaluated as the full width at half maximum of the point spread functions (**Supplementary Fig. 5**). We calibrated the FOV of miniBB2p by imaging a 50-μm grid standard (RTR1Ee-P, LBTEK). Field distortion due to optical aberrations (**Supplementary Fig. 2d**) and MEMS scan was corrected with the software *DistortionCleaner* (**Supplementary Figs. 4e-f**) [10]. All data in this study was displayed after distortion correction.

Tabletop Gaussian-beam 2PM. A tabletop Gaussian-beam 2PM (AX R MP, Nikon) with a water immersion objective (CFI Plan Fluor 10× W, NA 0.3, Nikon) was used to evaluate the performance of the miniBB2p. Lateral and axial resolution of the tabletop 2PM measured from 500-nm fluorescent beads were 1.34 ± 0.02 μm and 22.90 ± 0.47 μm (mean ± s.d., n = 5).

Animals. C57BL/6J male wild-type mice (Jackson Laboratory stock No. 000664) were obtained and housed at the Laboratory Animal Resource Center (LARC) within the Chinese Institute for Brain Research (CIBR). Thy1-GFP-M and VGAT-Cre transgenic mice were generously donated by Wenzhi Sun at CIBR. All mice were acquired at 5 weeks of age and allowed an average of 2 weeks to acclimate to their new environment before the experiments began. All experimental procedures were approved by the Institutional Animal Care and Use Committee of CIBR, in accordance with the governmental regulations of China.

Viral construction and packaging. Recombinant adeno-associated virus (rAAV) vectors were serotyped with AAV9 coat proteins and packaged at BrainCase viral vector manufacturing facilities. The viral titers were approximately 3.3×10^{12} particles per milliliter for rAAV2/9-CaMKIIα-hM4D(Gi)-mCherry and 5.2×10^{12} particles per milliliter for AAV-CaMKIIα-jGCaMP7f. Sparse expression was achieved by injecting a mixture of diluted AAV2/9-hSyn-Cre particles (original titer: ~1.3×10^{13} particles per milliliter, diluted 5,000-fold in sterilized phosphate-buffered saline) and high-titer, Cre-dependent GCaMP8s virus (rAAV2/9-hSyn-DIO-jGCaMP8s, 5.2×10^{13} infectious units per milliliter). Viral aliquots were stored in a light-protected freezer until use.

Surgical procedures. Mice were anesthetized with 1.5%-2% isoflurane, and viral vectors were delivered to the ACC, M2, or S1 regions of the brain. A fitted plunger controlled by a hydraulic manipulator (Beijing Xinglin Life Tech.) was inserted into a glass pipette to load and slowly inject 50 nL of viral vectors at a rate of 2 nL/5 s. Injections were performed bilaterally in the ACC at anteroposterior (AP) +1.3 mm, mediolateral (ML) ±0.3 mm, and dorsoventral (DV) -0.6 mm; bilaterally in S1 at AP -0.59 mm, ML ±1.5 mm, and DV -0.4 mm; and unilaterally in M2 at AP 0.6 mm, ML ±0.75 mm, and DV -0.5 mm. Following the injection, the microinjection needles were left in place for 10 minutes to allow viral diffusion and minimize the spread of viral particles along the injection tract. The pipette was then left in position for an additional 5 minutes before being slowly raised out of the brain.

After 3 weeks of expression, the mice were anesthetized with 1.5% isoflurane for cranial window implantation. Analgesic compound lidocaine cream was applied to the skin 10 minutes before the surgical incision, and ophthalmic ointment was used to prevent eye drying. The body temperature was maintained at 36°C using a feedback-controlled heating pad (FHC). A craniotomy with a diameter of 4.3 mm was performed over either the ACC or M2, leaving the dura intact. A glass coverslip of matching diameter was placed over the cranial window, and the gap between the glass window and the skull was sealed with Vetbond (3M, USA). After that, the isoflurane concentration was reduced to 0.5%-1%. The miniBB2p, with a custom titanium baseplate attached, was adjusted relative to the glass window to find the target plane for free-moving neural imaging. The baseplate was then secured with dental acrylic, and a custom cover was placed on the baseplate, fixed with screws, to protect the cranial window when not in use. Before surgery and testing, the mice were handled and pre-trained in the recording environment until they were acclimated and foraged freely within the box.

Imaging procedures. At the beginning of each imaging session, the mice were head-fixed and the miniBB2p was mounted on the baseplate. Behaviors of freely moving mice were recorded with a camera (MV-CS013-60GN, HIKROBOT) during entire experiment. Initially, spontaneous neural activity was recorded while the mice habituated to the testing environment, freely exploring the 30 cm × 20 cm × 20 cm recording chamber without any experimenter-delivered sensory stimuli.

For noxious stimulation, the plantar surface of the hind paw contralateral to the brain recording site was pricked with a 27-gauge needle (pin prick) while the mice were freely moving. The stimulation ceased upon the withdrawal of the paw. Non-noxious stimulation was delivered to the same hind paw using a 0.4 g von Frey filament, applied continuously for 3 seconds or until paw withdrawal. In most cases, there was no withdrawal response to the von Frey filament. Each recording session included approximately 10 trials with variable inter-trial

intervals of around 30 seconds to prevent sensitization. Throughout the sessions, no signs of behavioral sensitization or physical damage to the paws were observed.

Motion Correction and image analysis. To eliminate motion artifacts in the Ca^{2+} imaging data from each session, piecewise non-rigid motion correction was applied using *NoRMCorre* [25]. The motion-corrected 9 Hz calcium activity videos were saved as.TIFF files and subsequently used for cell identification.

For C57BL/6J mice injected with AAV-CaMKIIα-jGCaMP7f, calcium signals were extracted using *Suite2P*, which constrains the instances of calcium activity for each neuron [26]. The analysis produced three traces for each identified region of interest (ROI), corresponding to putative cell somata: the raw fluorescence signal $F_{cell}(t)$, the neuropil fluorescence signal $F_{np}(t)$, and the deconvolved calcium activity E(t). $F_{cell}(t)$ and $F_{np}(t)$ represent the weighted averages of activity within the ROI and the surrounding neuropil, respectively, excluding pixels overlapping with other ROIs. To correct for neuropil contamination, the neuropil signal was subtracted from the raw calcium signal using a fixed coefficient [27], yielding the corrected signal: $F_{corr}(t) = F_{cell}(t) - 0.7 \times F_{np}(t)$. To mitigate the effects of slow fluctuations such as photobleaching on F_{corr}, a running baseline $F_0(t)$ was extracted. The calcium activity was then expressed as the fractional change in fluorescence relative to the baseline ΔF/F, calculated as $\Delta F/F = (F_{corr}(t) - F_0(t)) / F_0(t)$.

For VGAT-Cre transgenic mice injected with rAAV2/9-hSyn-DIO-jGCaMP8s, the calcium imaging data from $VGAT^+$ cells were analyzed using the commercial image-analysis platform AIVIA 11.0 (DRVision Technologies LLC, Bellevue, WA) in conjunction with the *Cellpose* plugin. The segmentations from *Cellpose* were converted into masks for individual neurons, and the averaged fluorescent signal within each mask was used to calculate calcium transients.

Locomotion test. Custom-made dummy miniscopes (weighing 2.6 g) were utilized to assess the impact of miniBB2p on the behavior of mice during imaging. These dummies replicated the shape and weight distribution of the actual miniBB2p and were mounted onto implanted headbars, accompanied by one fiber and two cables. Each mouse was placed in a 40 cm × 40 cm × 40 cm box under 60 lux illumination, and its behavior was recorded for 10 minutes. The time spent, distance traveled in the central area (20 cm × 20 cm), and total distance traveled within the field were analyzed using a custom MATLAB (R2022b) program. The box was cleaned with 75% ethanol between tests.

Brain slice preparation. Mice were deeply anesthetized with isoflurane and then transcardially perfused with ice-cold phosphate-buffered saline (PBS) followed by paraformaldehyde (PFA). After extraction, the brains were fixed overnight in PFA. The fixed brains were then sectioned into 85 μm-thick slices using a vibratome (Leica VT1200S). These

brain slices were mounted onto slides using a mounting medium containing DAPI (Solarbio, China) to preserve the fluorescent signal for long-term storage.

Calcium response analyses. For the pain stimulation experiments, trial-averaged Ca^{2+} fluorescence traces were generated for individual neurons by z-scoring each trial from -5 to 5 seconds, with 0 indicating the time of stimulation. Z-scoring involved subtracting the mean and dividing by the standard deviation of a baseline period from -5 to -3 seconds prior to pinprick stimulation. The z-scored trials were then summed and divided by the total number of trials, resulting in a single trial-averaged Ca^{2+} fluorescence trace for each neuron.

To obtain a session-level analysis, trial-averaged Ca^{2+} fluorescence traces from individual neurons were combined and averaged across all neurons, producing a single representative trace of neuronal activity. The peak Ca^{2+} fluorescence for each neuron was identified within the post-stimulation window of 0 to 5 seconds. Each trial was z-scored as described, and then binned into 1-second intervals. A 2-second moving window was applied to determine the maximum average Ca^{2+} fluorescence for each trial. The peak values from all trials were then averaged to yield a singular value representing the peak post-stimulus activity of each neuron in a given session.

To evaluate the effect of running on neural activity in M2, we binarized the behavior of the mice into running/resting states and compared their mean ΔF/F values for each neuron. The running modulation index (MI) is calculated as $(\Delta F/F_{run} - \Delta F/F_{rest})/(\Delta F/F_{run} + \Delta F/F_{rest})$. A running onset was detected when a period of at least 400 ms of resting was followed by at least 400 ms of running [22]. For the investigation of neuronal response to running onsets, we inspected the ΔF/F responses with onsets that met two criteria simultaneously: (1) the onset had to be at least 10 seconds away from previous onset, and (2) the running episode had to last at least 1 second. This operation ensured that only well-separated and sustained running episodes were analyzed, minimizing the influence of transient or ambiguous movement signals.

Chemogenetics. Clozapine N-oxide (CNO; APExBIO, China) was prepared as a suspension in 0.9% saline, achieving a final concentration of 0.2 mg/mL. The solution was administered via intraperitoneal injection at a dose of 1 mg/kg. To activate the hM4D(Gi) DREADD, imaging was conducted 30 minutes following the systemic (intraperitoneal) injection of CNO.

Behavior tracking. The raw tracking video was initially analyzed using *DeepLabCut* (*DLC*) [28], which provided the positional data for specific body parts of the animal across each frame. Three key body parts were selected for analysis: the head, the body center, and the tail base. The *DLC* model was trained on a minimum of 20 frames, following the default training protocol, and underwent 30 thousand iterations. This training resulted in a final loss of approximately 0.003, with a training error of 1.48 pixels and a test error of 3.33 pixels. The animal's position

was recorded in x-y coordinates as x(t) and y(t). To smooth the positional traces, a low-pass filter was applied to both x(t) and y(t). The instantaneous movement speed was subsequently calculated by dividing the displacement of the head between consecutive frames by the time interval (1/frame rate), yielding a speed in centimeters per second (cm/s). Two-photon imaging was synchronized with the animal tracking camera in hardware, enabling precise temporal alignment between neuronal activity and behavioral tracking data. Calcium fluorescence traces were captured with the same number of frames as the tracking signals, ensuring that time points were pre-aligned across both datasets.

Statistical tests. For imaging data, paired neuronal recordings from a single session were compared using a paired Student's t-test, while unpaired data from separate sessions were analyzed using an unpaired Student's t-test. Changes in neuron populations before and after drug administration were assessed with Fisher's exact test. To determine pain-responsive neurons, a one-tailed Wilcoxon rank sum test was conducted on pre- and post-stimulus values for all peripheral stimulations during pain stimulus sessions, with significance set at $p < 0.025$. A similar one-tailed Wilcoxon rank sum test was employed to identify the neurons that responded to running onsets by comparing calcium activity during resting and running periods.

Data processing

Images were visualized and processed using the open-source software ImageJ. Unless stated otherwise, all images presented here were unprocessed raw images without smoothing, denoising, and deconvolution. “Green hot” lookup table in ImageJ was used for all miniBB2p captured images. Cross-section profiles, statistical graphs, and other coordinate graphs were drawn with Origin 2022 or MATLAB (R2022b). All neural activities and behaviors were collected at 9 and 27 fps, respectively. The supplementary videos were made at 25 fps using Adobe Premiere Pro 2024.

Data & code availability

The optical design files, technical drawings, and code for hardware control of miniBB2p are available in **Supplementary Data** (https://github.com/WuLab-CIBR/miniBB2p). Source data and code used for data processing are available from the corresponding author upon reasonable request.

Acknowledgments

This work was supported by the Innovation Fund for Medical Sciences from Chinese Academy of Medical Sciences (J. Wu), the startup funds from CIBR (J. Wu), the Beijing Municipal Science & Technology Commission (Z220009 to J. Wu), the National Natural Science Foundation of China (52205550 to L. Qian and 82401719 to Y. Liu). The authors thank the Behavior Analysis Center, Imaging Core, Instrumentation Core, Vector Core and LARC in CIBR for their support, and thank W. Z. Sun and M. M. Luo for constructive comments on the free-moving studies.

Contributions

J. Wu conceived the project and designed the optics; L. Qian designed the mechanics and electronics, L. Qian constructed the microscope; Y. Liu designed all animal research; Y. Liu and L. Qian collected data; Y. Liu, L. Qian, and Y. Chen analyzed data; J. Wu supervised research; J. Wu, Y. Liu, and L. Qian wrote the manuscript with inputs from all authors.

Conflict of interests

The authors declare no competing interests.

REFERENCES

1. Helmchen, F., Fee, M.S., Tank, D.W., and Denk, W. A miniature head-mounted two-photon microscope: high-resolution brain imaging in freely moving animals. Neuron **31**, 903–912 (2001). https://doi.org/10.1016/s0896-6273(01)00421-4

2. Zong, W., Wu, R., Li, M. et al. Fast high-resolution miniature two-photon microscopy for brain imaging in freely behaving mice. Nat. Methods **14**, 713–719 (2017). https://doi.org/10.1038/nmeth.4305

3. Ozbay, B.N., Futia, G.L., Ma, M. et al. Three dimensional two-photon brain imaging in freely moving mice using a miniature fiber coupled microscope with active axial-scanning. Sci. Rep. **8**, 8108 (2018). https://doi.org/10.1038/s41598-018-26326-3

4. Klioutchnikov, A., Wallace, D.J., Frosz, M.H. et al. Three-photon head-mounted microscope for imaging deep cortical layers in freely moving rats. Nat. Methods **17**, 509–513 (2020). https://doi.org/10.1038/s41592-020-0817-9

5 Zong, W., Wu, R., Chen, S. et al. Miniature two-photon microscopy for enlarged field-of-view, multi-plane and long-term brain imaging. Nat. Methods **18**, 46–49 (2021). https://doi.org/10.1038/s41592-020-01024-z

6 Klioutchnikov, A., Wallace, D.J., Sawinski, J. et al. A three-photon head-mounted microscope for imaging all layers of visual cortex in freely moving mice. Nat. Methods **20**, 610–616 (2023). https://doi.org/10.1038/s41592-022-01688-9

7 Zhao, C., Zhu, Y., Zhang, D. et al. Millimeter field-of-view miniature two-photon microscopy for brain imaging in freely moving mice. Opt. Express **31**. 32925–32934(2023). https://doi.org/10.1364/OE.492674

8 Zhao, C., Chen, S., Zhang, L. et al. Miniature three-photon microscopy maximized for scattered fluorescence collection. Nat. Methods **20**, 617–622 (2023). https://doi.org/10.1038/s41592-023-01777-3

9 Madruga, B.A., Dorian, C.C., Sehgal, M. et al. Open-source, high performance miniature multiphoton microscopy systems for freely behaving animals. Preprint at bioRxiv (2024). https://doi.org/10.1101/2024.03.29.586663

10 Zong, W., Obenhaus, H.A., Skytøen, E.R. et al. Large-scale two-photon calcium imaging in freely moving mice. Cell **185**, 1240–1256 (2022). https://doi.org/10.1016/j.cell.2022.02.017

11 Obenhaus, H.A., Zong, W., Jacobsen, R.I. et al. Functional network topography of the medial entorhinal cortex. Proc. Natl. Acad. Sci. U. S. A. **119**, e2121655119 (2022). https://doi.org/10.1073/pnas.2121655119

12 Zhang, C., Zhu, H., Ni, Z. et al. Dynamics of a disinhibitory prefrontal microcircuit in controlling social competition. Neuron **110**, 516–531(2022). https://doi.org/10.1016/j.neuron.2021.10.034

13 Chen, X., Liu, Y., Xu, N., and Sun. Y. Itch perception is reflected by neuronal ignition in the primary somatosensory cortex. Natl. Sci. Rev. **9**, nwab218 (2022). https://doi.org/10.1093/nsr/nwab218

14 Griffiths, V.A., Valera, A.M., Lau, J.Y. et al. Real-time 3D movement correction for two-photon imaging in behaving animals. Nat. Methods **17**, 741–748 (2020). https://doi.org/10.1038/s41592-020-0851-7

15 Botcherby, E.J., Juškaitis, R. and Wilson, T. Scanning two photon fluorescence microscopy with extended depth of field. Opt. Commun. **268**, 253–260 (2006). https://doi.org/10.1016/j.optcom.2006.07.026

16 Thériault, G., De Koninck, Y., and McCarthy, N. Extended depth of field microscopy for rapid volumetric two-photon imaging. Opt. Express **21**, 10095–10104 (2013). https://doi.org/10.1364/OE.21.010095

17 Lu, R., Sun, W., Liang, Y. et al. Video-rate volumetric functional imaging of the brain at synaptic resolution. Nat. Neurosci. **20**, 620–628 (2017). https://doi.org/10.1038/nn.4516

18 Meng, G., Liang, Y., Sarsfield, S. et al. High-throughput synapse-resolving two-photon fluorescence microendoscopy for deep-brain volumetric imaging in vivo. eLife **8**, e40805 (2019). https://doi.org/10.7554/eLife.40805

19 Lu, R., Liang, Y., Meng, G. et al. Rapid mesoscale volumetric imaging of neural activity with synaptic resolution. Nat. Methods **17**, 291–294 (2020). https://doi.org/10.1038/s41592-020-0760-9

20 Chen, W., Natan, R.G., Yang, Y. et al. In vivo volumetric imaging of calcium and glutamate activity at synapses with high spatiotemporal resolution. Nat. Commun. **12**, 6630 (2021). https://doi.org/10.1038/s41467-021-26965-7

21 Tanaka, T. and Yamamoto, S. Comparison of aberration between axicon and lens. Opt. Commun. **184**, 113–118 (2000). https://doi.org/10.1016/S0030-4018(00)00963-9

22 Ayaz, A., Stäuble, A., Hamada, M. et al. Layer-specific integration of locomotion and sensory information in mouse barrel cortex. Nat. Commun. **10**, 2585 (2019). https://doi.org/10.1038/s41467-019-10564-8

23 Zhang, Q., Manders, T., Tong, A.P. et al. Chronic pain induces generalized enhancement of aversion. eLife **6**, e25302 (2017). https://doi.org/10.7554/eLife.25302

24 Singh, A., Patel, D., Li, A. et al. Mapping cortical integration of sensory and affective pain pathways. Curr. Biol. **30**, 1703-1715 (2020). https://doi.org/10.1016/j.cub.2020.02.091

25 Pnevmatikakis, E.A. and Giovannucci, A. NoRMCorre: An online algorithm for piecewise rigid motion correction of calcium imaging data. J. Neurosci. Methods **291**, 83-94 (2017). https://doi.org/10.1016/j.jneumeth.2017.07.031

26 Pachitariu, M., Stringer, C. et al. Suite2p: beyond 10,000 neurons with standard two-photon microscopy. Preprint at bioRxiv (2017). https://doi.org/10.1101/061507

27 Pachitariu, M., Stringer, C. and Harris, K.D. Robustness of spike deconvolution for neuronal calcium imaging. J. Neurosci. **38**, 7976-7985 (2018). https://doi.org/10.1523/JNEUROSCI.3339-17.2018

28 Mathis, A., Mamidanna, P., Cury, K.M. et al. DeepLabCut: markerless pose estimation of user-defined body parts with deep learning. Nat. Neurosci. **21**, 1281–1289 (2018). https://doi.org/10.1038/s41593-018-0209-y

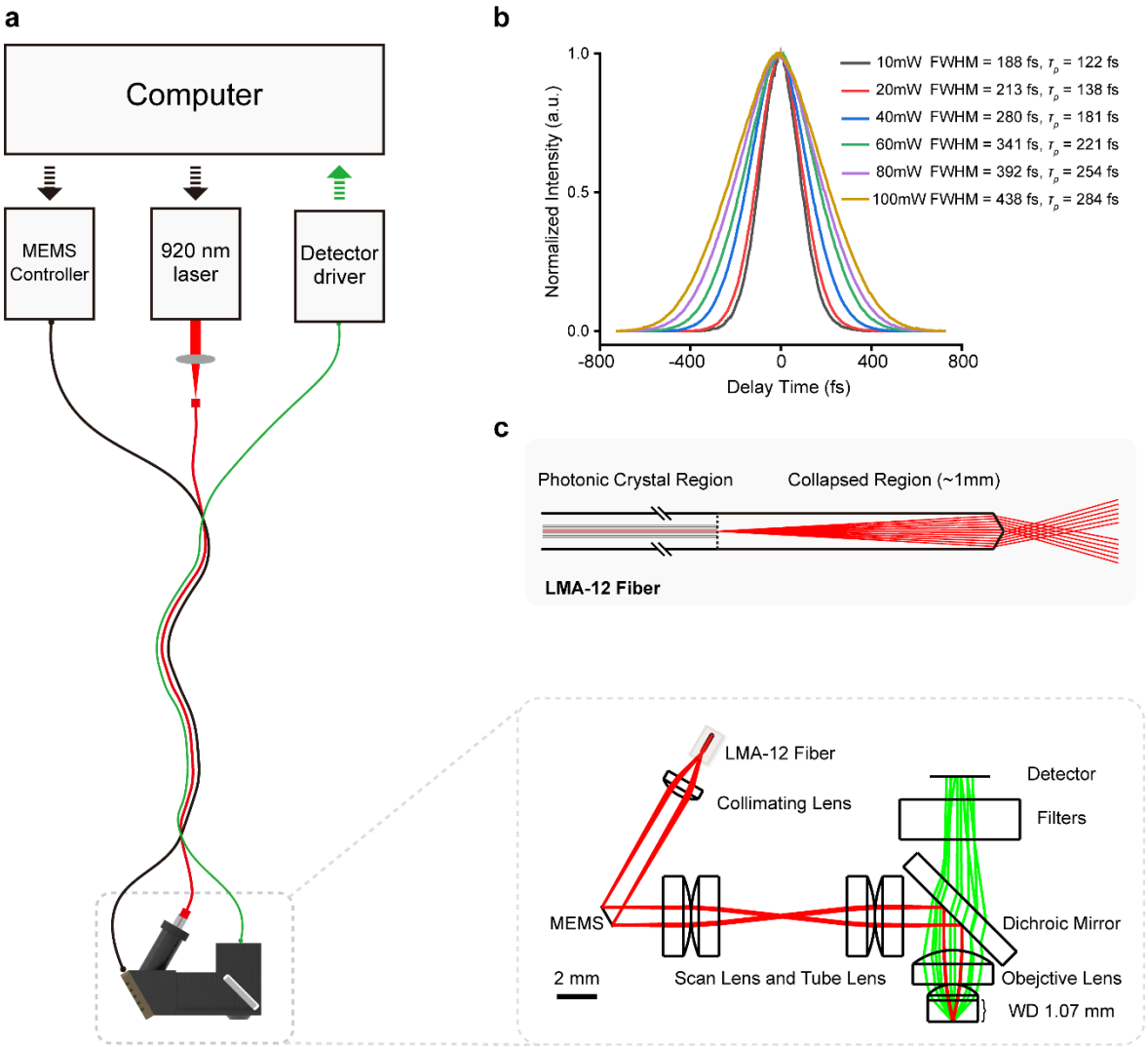

Supplementary Fig. 1 | Design of miniBB2p and pulse delivery test. a, Overview of miniBB2p; inset, optical layout of miniBB2p headpiece; WD, working distance. **b**, Autocorrelation traces from an autocorrelator (FR-103HP, Femtochrome) showing the widths of 920-nm laser pulses after passing through a 1-meter LMA-12 fiber at different powers. The pulse width (τ_p) is calculated as ~0.65 times the width of the autocorrelation signal, assuming the pulse is shaped like a sech² function, which is typical in mode-locked lasers. FWHM, full width at half maximum. **c**, Schematic of the photonic crystal fiber LMA-12 with a custom axicon at the tip.

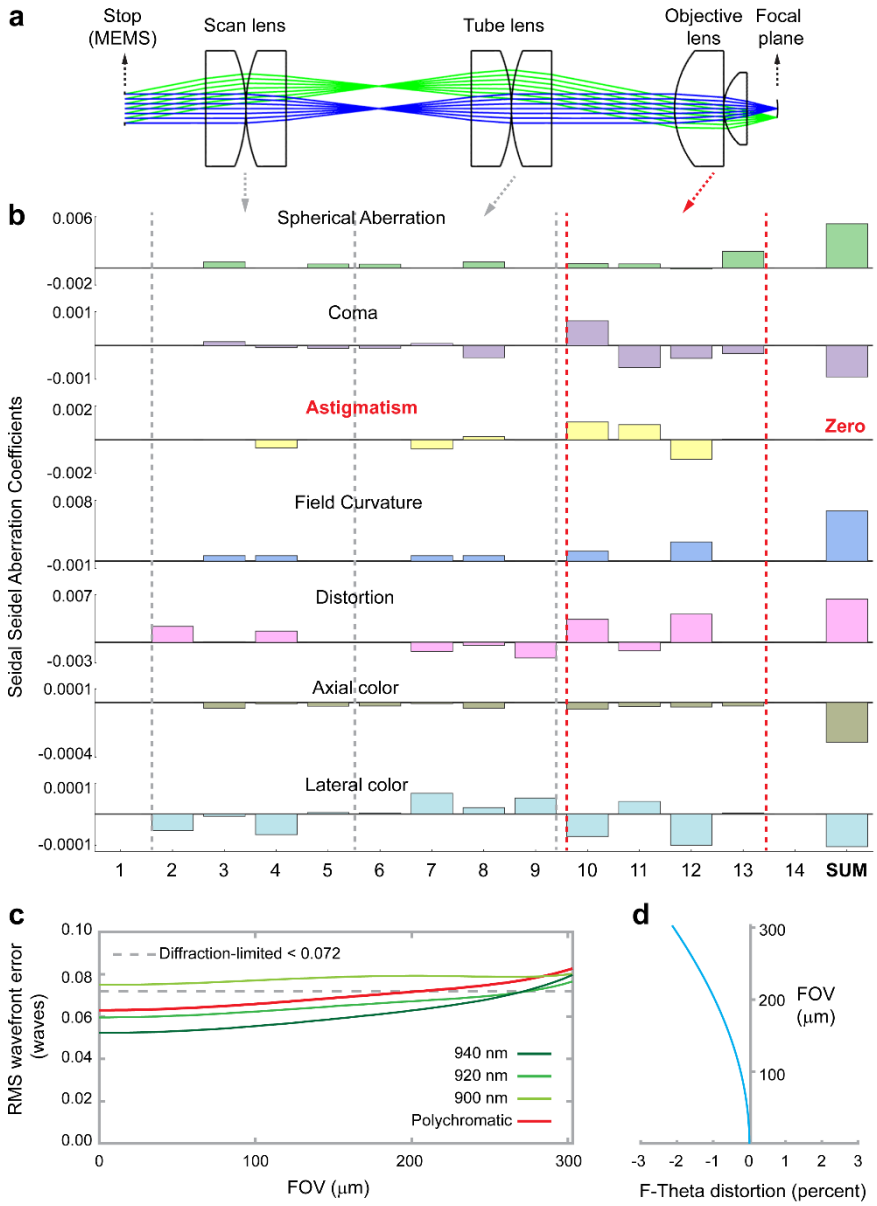

Supplementary Fig. 2 | Excitation optics in miniBB2p. a, Unfolded excitation beam path from the MEMS mirror to focal plane. Blue and green rays represent the beam focusing at the center and edge of the FOV. Note that the focal plane is curved with a radius of 2 mm, resulting in a maximum focal shift of ~10 μm across the entire FOV. **b**, Seidel aberration coefficients across lenses. **c**, Root-mean-square wavefront error throughput a FOV of Ø 600 μm. **d**, Distortion of the microscope; maximum distortion is ~ -2.1%. The stop size is 1 mm and NA is 0.3 in the simulation (See optical design files in **Supplementary Data**).

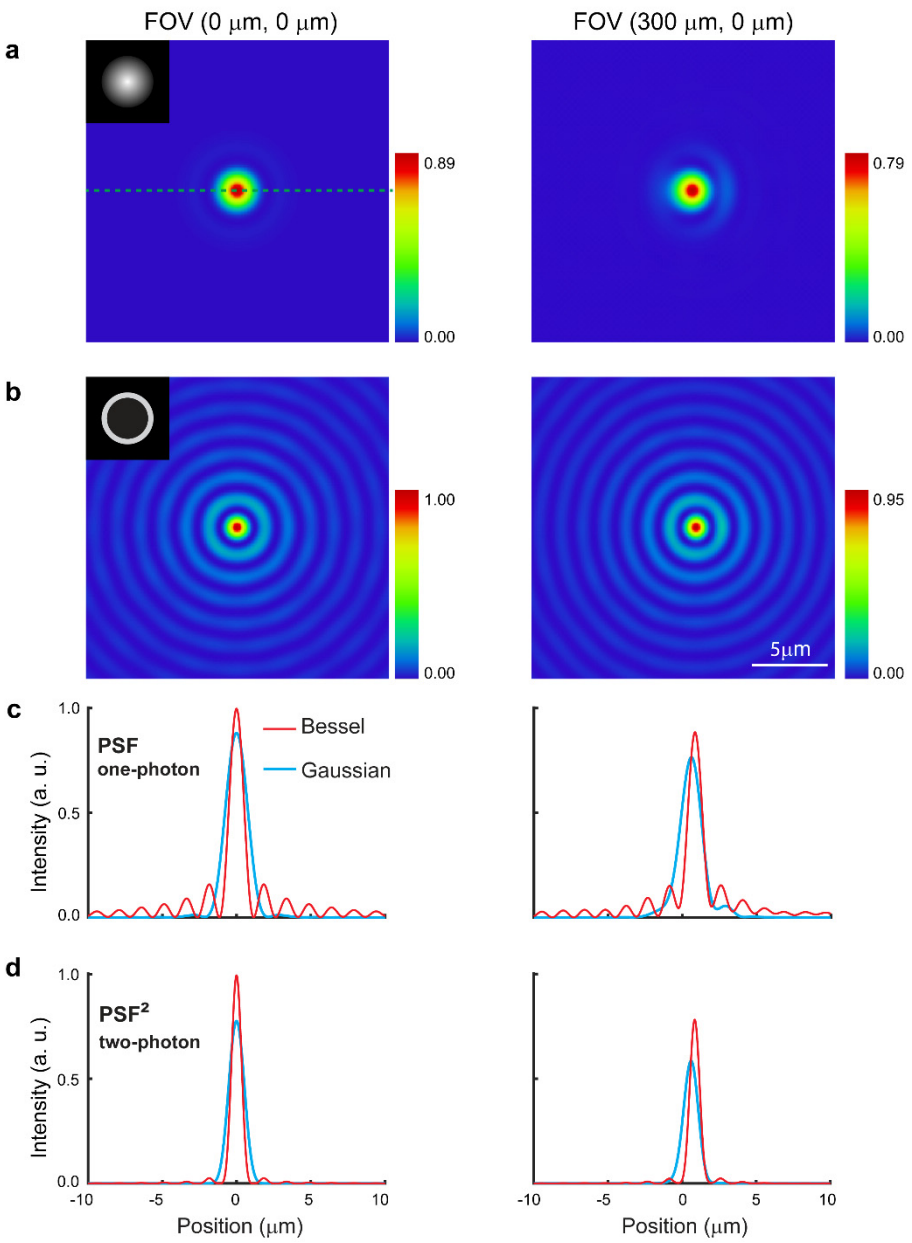

Supplementary Fig. 3 | Simulation of miniBB2p with Gaussian and Bessel beam excitation. **a**, Gaussian focus at the focal plane; inset, beam diameter at the stop is 1 mm (NA=0.3). **b**, Bessel focus at the focal plane; inset, annular aperture at the stop, outer and inner diameters are 1 mm and 0.98 mm (NA=0.3). **c-d**, Lateral point spread function (PSF) with Gaussian and Bessel beam excitation, **c**, one-photon; **d**, two-photon. Maximum intensity of an unaberrated PSF is 1. Left and right panels compare their performance at the center and edge of the FOV.

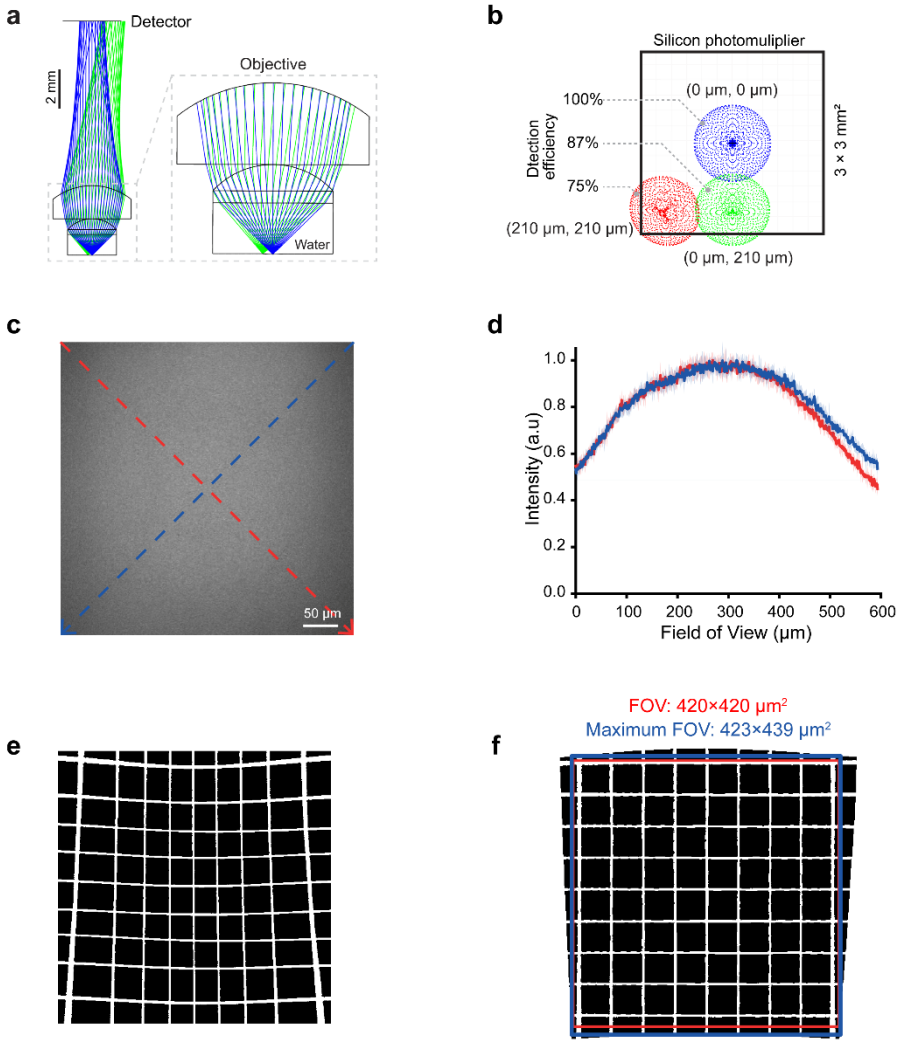

Supplementary Fig. 4 | Fluorescence collection and distortion correction in miniBB2p. a, Ray path from the focal plane to the detector; zoom-in view shows the ray path in the objective; fluorescence collection NA is 0.95; dichroic mirror and filters are omitted for simplicity. Blue and green rays illustrate fluorescence from the center and edge of the FOV. **b**, Fluorescence from different locations detected by the silicon photomultiplier. The simple optics in miniBB2p enabled highest detection efficiency in the center and an acceptable detection efficiency at the edge (87%) and corner (75%) of the FOV. **c**, Field uniformity tested with a fluorescent plastic slide (92001, Chroma). **d**, Normalized fluorescence intensity across the diagonal lines in **c** (average from ten images, shaded areas show standard deviation). **e-f**, Bright field image of a 50-μm grid standard before (**e**) and after (**f**) distortion correction (see **Resolution and FOV calibration** in **Methods**); image was captured without the filters installed in miniBB2p.

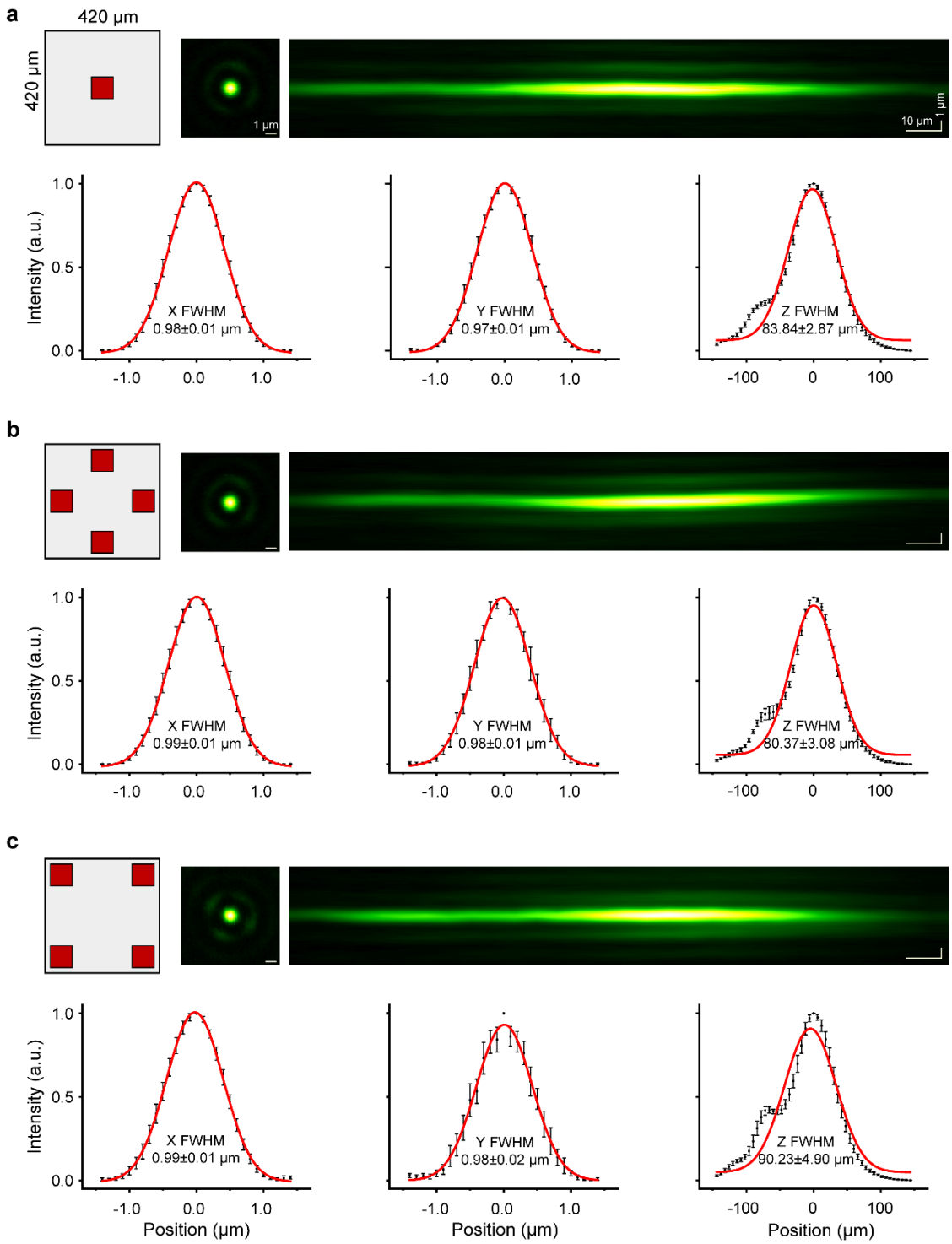

Supplementary Fig. 5 | Lateral and axial resolution in miniBB2p. PSF at the center (**a**); edge (**b**), and corner (**c**) of the FOV. Top: illustration of the positions for measuring resolution, representative image and side projection of a 500-nm fluorescent bead. Bottom: PSF profiles; the resolutions were evaluated as the FWHM of the PSFs (mean ± s.d., n = 10).

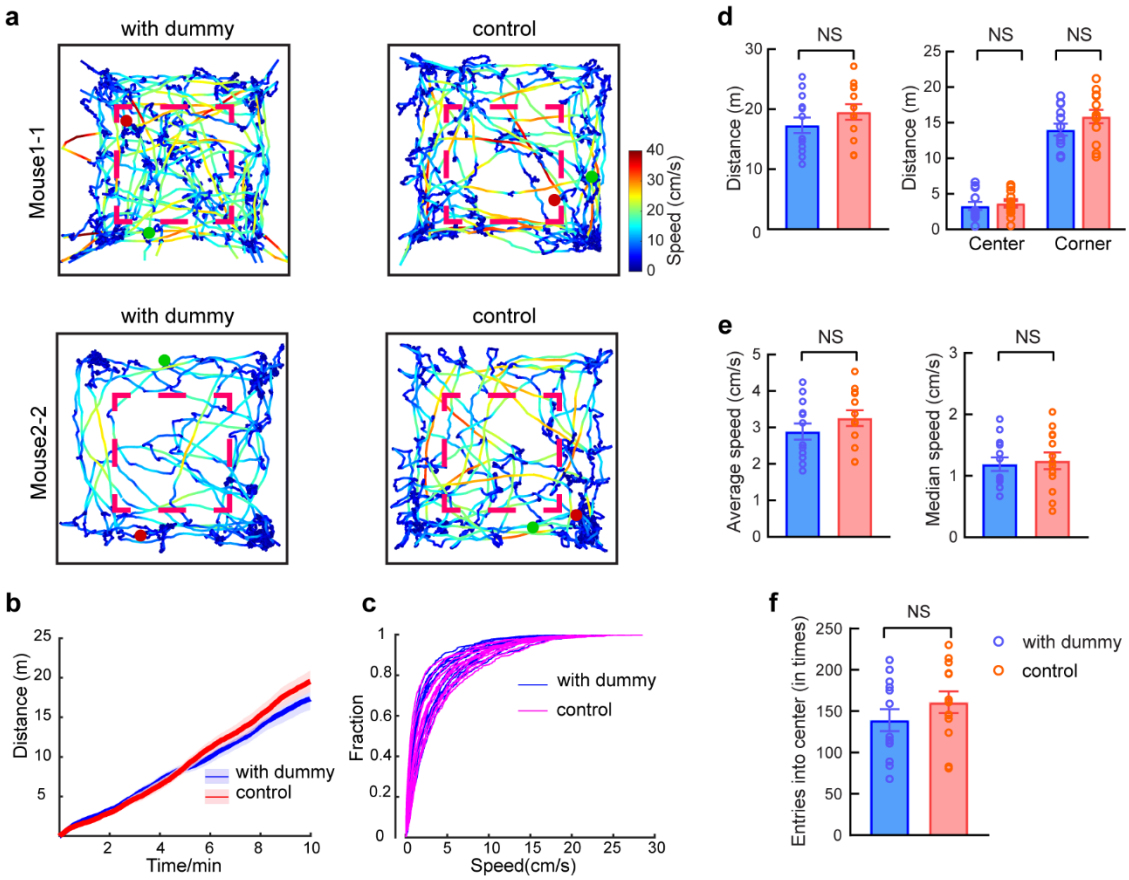

Supplementary Fig. 6 | Minimal impact of miniBB2p on mice movement. a, Two example mouse trajectories extracted from the videos of 10-min test sessions with and without dummy. The line denotes the path taken; the red dot marks the origin, and the green dot marks the end. The colors code the moving speeds. **b**, Accumulated distance over 10 min of running; average from 10 mice, shaded areas show s.e.m. **c**, Cumulative speed distribution over 10 min of running. Each curve shows one trial. **d**, Total distance traveled (left), distance traveled in central 20 cm square and corner (right) in each condition (10 min each). No significant differences were found ($p = 0.2826$ for total distance; $p = 0.6565$ for center distance; $p = 0.1787$ for corner distance, paired t test). **e**, Average speed (left) and median speed (right) in each condition (10 min each). No significant differences were found both in average speed ($p = 0.3288$, paired t test) and median speed ($p = 0.7831$, paired t test). **f**, Number of entries into the central 20 cm square. No significant differences were found ($p = 0.3288$, paired t test). Data in **d-f** are presented as mean ± s.e.m.

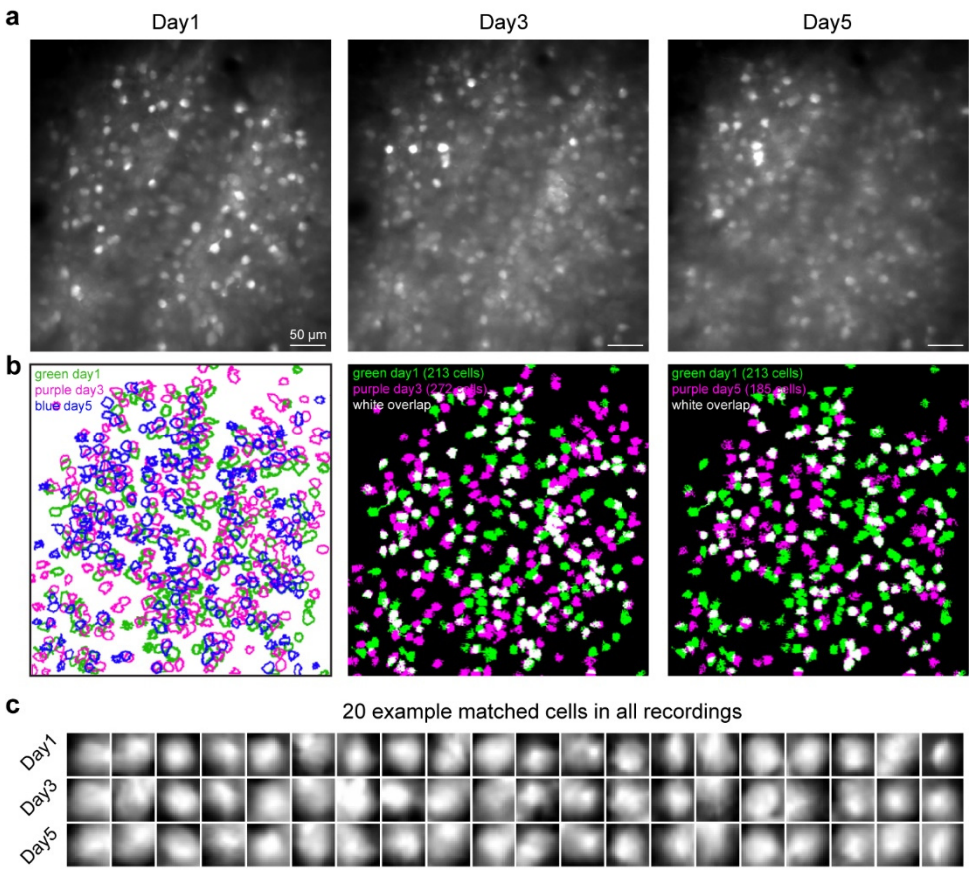

Supplementary Fig. 7 | Stability of miniBB2p imaging. **a**, Recording same FOV of ACC on different days. **b**, Matched cell candidates were automatically detected with a MATLAB package (Adam Ranson, https://github.com/ransona/ROIMatchPub) by setting an overlap ratio (50% in this analysis); morphological structure of matched cells was manually checked for filtering out unreliable cell pairs. 43.7% of the cells could be matched between the first and last recording, and 50 cells (23.4% of the cells recorded in day 1) could be matched across all recordings. **c**, 20 example cells identified across all recordings, showing similar cell morphology.

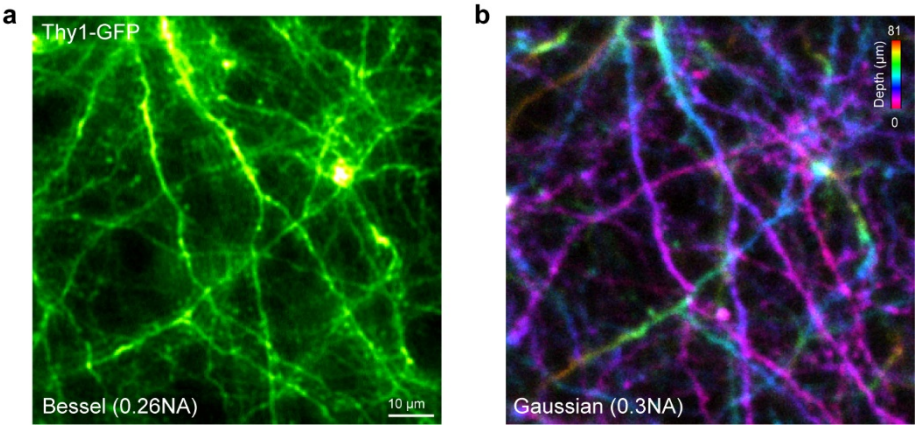

Supplementary Fig. 8 | Imaging of dendrites and spines in the head-fixed awake Thy1-GFP mouse brain. a, Image of a ~80-µm thick volume in ACC by miniBB2p. **b**, An image stack at 3-µm step collected by the tabletop Gaussian beam 2PM from same volume, with structures colored by depth.

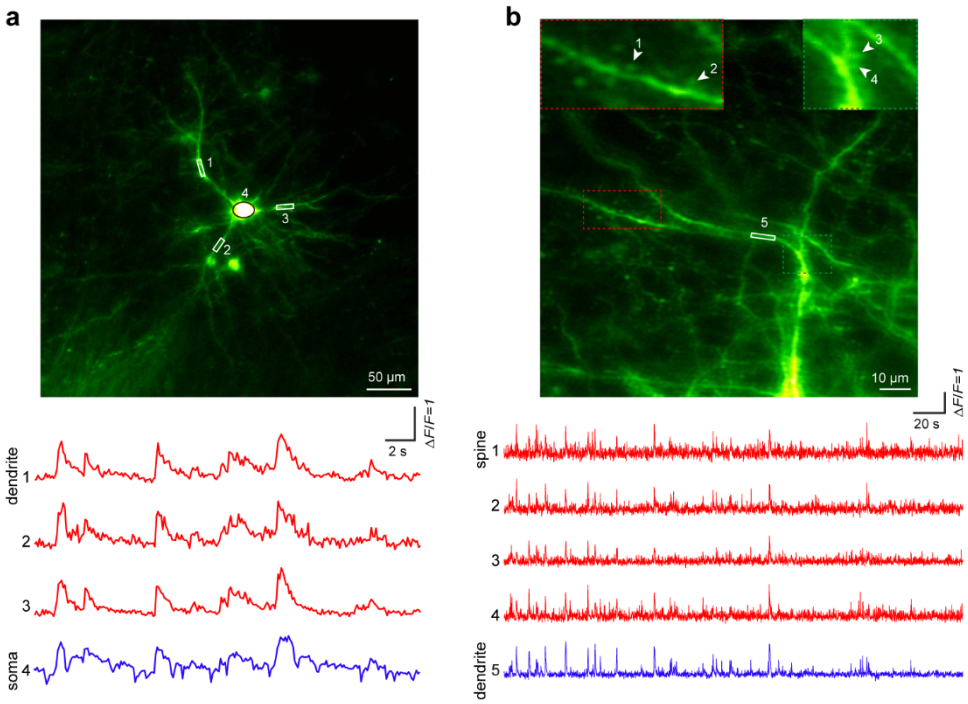

Supplementary Fig. 9 | Imaging the activities of dendrites and spines in mice brain expressing GCaMP8s by miniBB2p. a, FOV, 420 × 420 μm^2; ACC in a head-fixed awake mouse. **b**, FOV, 120 × 120 μm^2; ACC in a freely moving mouse; insets show zoom-in views of the color boxed areas.

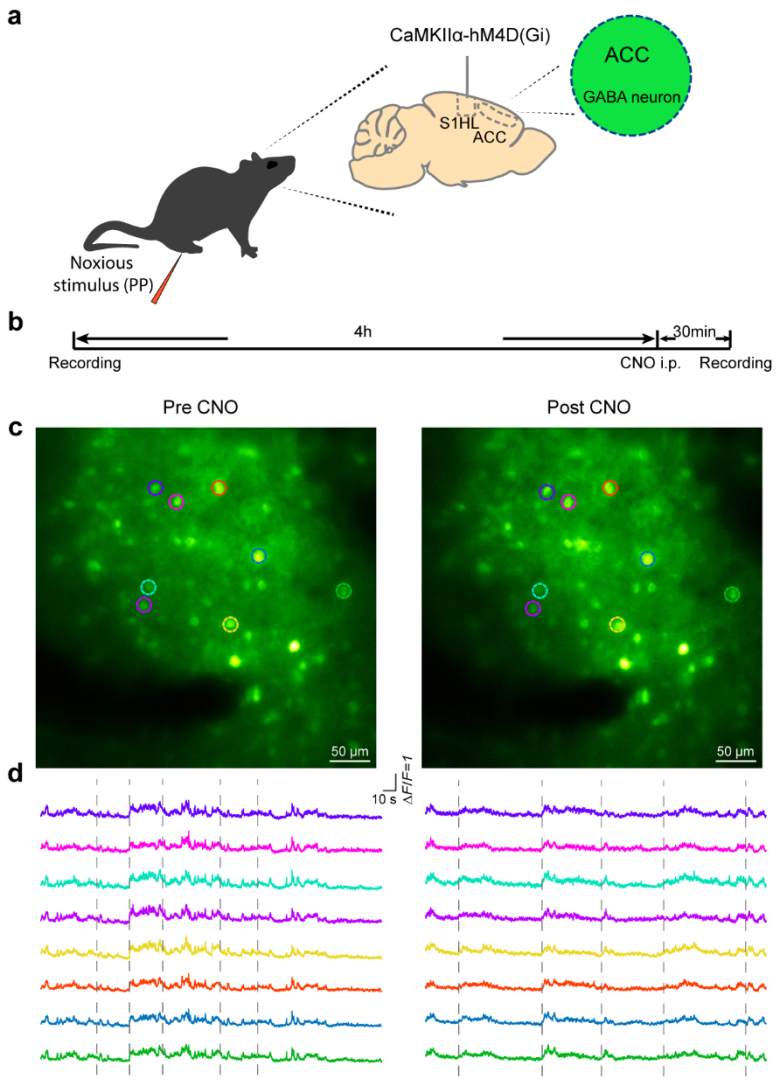

Supplementary Fig. 10 | Inhibition of S1 inputs enhance the nociceptive response in ACC. **a-b**, Schematic of the experiment. **c**, Imaging in ACC before and after CNO injection using miniBB2p. **d**, ΔF/F traces of neurons outlined in **c**; dashed lines indicate the time points of pin prick.

Supplementary Table 1: Optical performance in the state-of-the-art miniature multiphoton microscopes

Reference	Klioutchnikov, A. et al. *Nat Methods* (2020)	Klioutchnikov, A. et al. *Nat Methods* (2023)	Zhao, C. et al. *Nat Methods* (2023)	Zhao, C. et al. *Opt Express* (2023)	Zong, W. et al. *Cell* (2022)	Madruga, B.A. et al. *bioRxiv* (2024)	This work
Lens architecture **Excitation** **Collection**	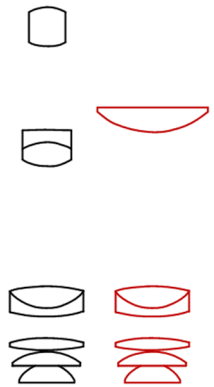	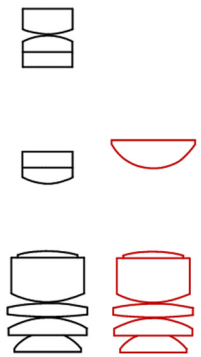	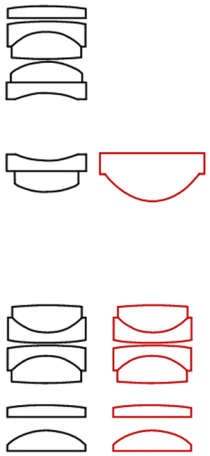	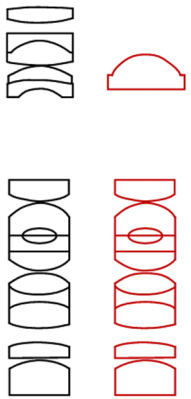	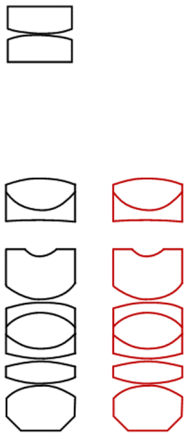	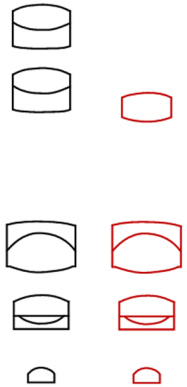	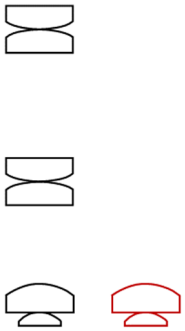
Modality (2p/3p)	3p	3p	3p	2p	2p	2p	2p
Collection NA	0.9	0.9	0.65	0.45	0.45-0.5	0.56	0.95
Excitation NA	0.48-0.54	0.48 / 0.58	0.55	0.25	0.45-0.5	0.36	0.26
Lateral resolution	0.8 μm	1.18 / 1.11 μm	0.97-1.21 μm	1.47 μm	1.15-1.24 μm	0.98 μm	0.97-0.99 μm
Axial resolution (depth of field)	5.3 μm	13.8 / 10.1 μm	7.21-8.51 μm	24.64 μm	12.8-17.8 μm	10.18 μm	80.37-90.23 μm
FOV	160 × 160 μm^2	300 × 300 / 200 × 200 μm^2 *	400 × 400 μm^2	1000 × 788 μm^2	420 × 420 / 500 × 500 μm^2 **	445 x 380 μm^2	423 × 439 μm^2
Frame rate	27.78 Hz @ 120 × 120 pixels	10.6 Hz @ 273 × 280 pixels	15.93 / 8.35 Hz @ 128 × 128 / 200 × 200 pixels	9 Hz @ 600 × 512 pixels	40 / 15 Hz @ 256 × 256 pixels	not mentioned	9 Hz @ 512 × 512 pixels

Note: Major developments after 2020 with a known lens structure were listed here.

* Two configurations: extended z-range with 0.48 NA, 300 × 300 μm^2 FOV; high-resolution with 0.58 NA, 200 × 200 μm^2 FOV.

** Two configurations: MINI2P-F with 420 × 420 μm^2 FOV, 40 Hz frame rate; MINI2P-L with 500 × 500 μm^2 FOV, 15 Hz frame rate.

Supplementary Table 2: Major parameters used for miniBB2p imaging

	Indicator	Paradigm	Microscope	FOV (μm^2)	Frame rate	Imaging duration	3D data projection*	Laser power (mW)**
Fig. 1f (Left)	Thy1-GFP	Brain slice	miniBB2p	400 × 400	9 Hz	11.1 s (100 frames)	mean	80
Fig. 1f (Right)	Thy1-GFP	Brain slice	Tabletop 2P	400 × 400	1.9 Hz	14.7 s (28 images)	sum	25
Fig. 1g (Left)	Thy1-GFP	Brain slice	miniBB2p	60 × 60	9 Hz	11.1 s (100 frames)	mean	80
Fig. 1g (Right)	Thy1-GFP	Brain slice	Tabletop 2P	60 × 60	0.16 Hz	176 s (28 images)	sum	25
Fig. 1h, Video S1	GCaMP7f	Free-moving	miniBB2p	423 × 439	9 Hz	6 min 10 s	s.d.	40
Fig. 1k	GCaMP7f	Head-fixed	Tabletop 2P	423 × 439	0.8 Hz	35 s (28 images)	sum	12
Fig. 1l	GCaMP7f	Head-fixed	Tabletop 2P	423 × 439	7.7 Hz	6 min (2 min/layer)	mean	9
Fig. 2a Video S4	GCaMP7f	Free-moving	miniBB2p	420 × 420	9 Hz	30 min	s.d.	40
Fig. 2h Video S5	GCaMP7f	Free-moving	miniBB2p	420 × 420	9 Hz	8 min	s.d.	40
Fig. S7	GCaMP7f	Head-fixed	miniBB2p	423 × 439	9 Hz	5 min	s.d.	40
Fig. S8 (Left)	Thy1-GFP	Head-fixed	miniBB2p	90 × 90	9 Hz	6.7 s (60 frames)	mean	80
Fig. S8 (Right)	Thy1-GFP	Head-fixed	Tabletop 2P	90 × 90	1.9 Hz	14.7 s (28 images)	sum	25
Fig. S9a Video S2	GCaMP8s	Head-fixed	miniBB2p	420 × 420	9 Hz	27 s	mean	80
Fig. S9b Video S3	GCaMP8s	Free-moving	miniBB2p	120 × 120	9 Hz	5 min 4 s	mean	100
Fig. S10 (Left)	GCaMP8s	Free-moving	miniBB2p	420 × 420	9 Hz	4 min 40 s	mean	60
Fig. S10 (Right)	GCaMP8s	Free-moving	miniBB2p	420 × 420	9 Hz	3 min 47 s	mean	60

* Various z-projection methods were used for the presentation of the 3D data

** Laser power is measured after the objective lens

Supplementary Table 3: Cost of the miniBB2p headpiece

Component	Manufacturer	Part number /Name	Quantity	Note	Cost	Subtotal
Objective lens	Edmund	47-850	1		$67	$145
	Edmund	65-300	1		$78	
Scan and tube lenses	Edmund	48-704	4		$58	$232
Collimating lens	Edmund	45-956	1		$76.5	$76.5
Dichroic mirror	LBTEK	DMR-805SP	1	¥2844, Can cut into 12 pieces of 7 × 7 mm^2	$391.58	$391.58
Filters	Sunlight	FIL-800	1	¥643	$88.53	$177.42
	Thorlabs	FGB37-A	1	Can cut into 5 pieces of 6 × 6 mm^2	$88.89	
MEMS mirror	Mirrorcle	A3I12.2-1200AL	1		$590	$590
Fiber and axicon tip	NKT Photonics	LMA-12	1 m		$170	$307.69
	Comcore	Custom	1	¥1000	$137.69	
Glass flange	Sunlight	TUB-1.8x6-0.127	1	¥30	$4.13	$4.13
Mechanical housings	Custom	Objective Holder	1	¥250	$34.42	$268.49
		Scan and Tube Lens Holder	1	¥350	$48.19	
		Collimating Lens Holder	1	¥350	$48.19	
		Main Frame	1	¥1000	$137.69	
SiPM detector	Hamamatsu	S13360-3075PE	1		$62.23	$62.23
In total						**$2255.04**

Note: These costs were as of July 2024 when components were purchased at small scale, with the exchange rate of 7.26 RMB to 1 USD. The costs contained the key components of the headpiece, but did not include additional hardware, such as laser, digitizer, PC, etc.

SUPPLEMENTARY VIDEO INFORAMTION

Supplementary Video 1：Imaging the neural activities in ACC in a freely moving mouse. Images were captured at 9 frames per second, 423 × 439 μm^2 FOV, and 40 mW post-objective power. Data were corrected for motion artifacts, binned every 3 frames, and saved at 25 binned frames per second (top left). Behavior video of the mouse in the chamber during imaging (top right). Calcium traces of example neurons (bottom).

Supplementary Video 2: Imaging the activities of dendritic trees in ACC in a head-fixed awake mouse. Images were captured at 9 frames per second, 420 × 420 μm^2 FOV, and 80 mW post-objective power. Data were corrected for motion artifacts and saved at 25 frame per second.

Supplementary Video 3: Imaging the activities of dendrites and spines in ACC in a freely moving mouse. Images were captured at 9 frames per second, 120 × 120 μm^2 FOV, and 100 mW post-objective power. Data were corrected for motion artifacts, binned every 3 frames, and saved at 25 binned frames per second

Supplementary Video 4: Imaging the neural activities in M2 in a freely moving mouse over a 30-minute period. Images were captured at 9 frames per second, 420 × 420 μm^2 FOV, and 40 mW post-objective power. Data were corrected for motion artifacts, binned every 9 frames, and saved at 25 binned frames per second (top left). Behavior video of the mouse in the chamber during imaging (top right). Calcium traces of example neurons (bottom left) and movement trajectory of the mouse (bottom right)

Supplementary Video 5: Imaging the response of ACC neurons to pain stimulus in a freely moving mouse. Images were captured at 9 frames per second, 420 × 420 μm^2 FOV, and 40 mW post-objective power. Data were corrected for motion artifacts, binned every 3 frames, and saved at 25 binned frames per second (left). Behavior video of the mouse under non-noxious and noxious stimulus (right).